

Article

The $\text{Zn}_{1-x}\text{Pb}_x\text{Cr}_2\text{Se}_4$ —Single Crystals Obtained by Chemical Vapour Transport—Structure and Magnetic, Electrical, and Thermal Properties

Izabela Jendrzejewska ^{1,*}, Tadeusz Groń ², Joachim Kusz ², Zbigniew Stokłosa ³, Ewa Pietrasik ¹, Tomasz Goryczka ³, Bogdan Sawicki ², Jerzy Goraus ², Josef Jampilek ⁴, Henryk Duda ² and Beata Witkowska-Kita ⁵

¹ Institute of Chemistry, University of Silesia in Katowice, 40-007 Katowice, Poland; ewa.pietrasik@us.edu.pl

² Institute of Physics, University of Silesia in Katowice, 40-007 Katowice, Poland; tadeusz.gron@us.edu.pl (T.G.); joachim.kusz@us.edu.pl (J.K.); bogdan.sawicki@us.edu.pl (B.S.); jerzy.goraus@us.edu.pl (J.G.); henryk.duda@us.edu.pl (H.D.)

³ Institute of Materials Science, University of Silesia in Katowice, 40-007 Katowice, Poland; zbigniew.stoklosa@us.edu.pl (Z.S.); tomasz.goryczka@us.edu.pl (T.G.)

⁴ Faculty of Natural Sciences, Comenius University, 842 15 Bratislava, Slovakia; josef.jampilek@gmail.com

⁵ Katowice Branch, Research Network Łukasiewicz—Institute of Mechanised Construction and Rock Mining, 02-673 Warszawa, Poland; b.witkowskakita@gmail.com

* Correspondence: izabela.jendrzejewska@us.edu.pl

Abstract: Monocrystalline chalcogenide spinels ZnCr_2Se_4 are antiferromagnetic and semiconductor materials. They can be used to dope or alloy with related semiconducting spinels. Therefore, their Pb-doped display is expected to have unique properties and new potential applications. This paper presents the results of dc and ac magnetic measurements, including the critical fields visible on the magnetisation isotherms, electrical conductivity, and specific heat of the $\text{ZnCr}_2\text{Se}_4\text{:Pb}$ single crystals. These studies showed that substituting the diamagnetic Pb ion with a large ion radius for the Zn one leads to strong short-range ferromagnetic interactions in the entire temperature range and spin fluctuations in the paramagnetic region at $H_{dc} = 50$ kOe.

Keywords: chalcogenides; X-ray study; magnetic and electrical properties; specific heat; thermal analysis

Citation: Jendrzejewska, I.; Groń, T.; Kusz, J.; Stokłosa, Z.; Pietrasik, E.; Goryczka, T.; Sawicki, B.; Goraus, J.; Jampilek, J.; Duda, H.; et al. The $\text{Zn}_{1-x}\text{Pb}_x\text{Cr}_2\text{Se}_4$ —Single Crystals Obtained by Chemical Vapour Transport—Structure and Magnetic, Electrical, and Thermal Properties. *Materials* **2022**, *15*, 5289. <https://doi.org/10.3390/ma15155289>

Academic Editor: Lei Zhang

Received: 5 June 2022

Accepted: 27 July 2022

Published: 31 July 2022

Publisher's Note: MDPI stays neutral with regard to jurisdictional claims in published maps and institutional affiliations.



Copyright: © 2022 by the authors. Licensee MDPI, Basel, Switzerland. This article is an open access article distributed under the terms and conditions of the Creative Commons Attribution (CC BY) license (<https://creativecommons.org/licenses/by/4.0/>).

1. Introduction

Magnetic and semiconductor spinels are of great interest because of their exotic phenomena and the fascinating ground states observed at the turn of the 20th and 21st centuries, such as [1]: behaviour of heavy fermions [2,3], complex spin order and spin dimerization [4–6], spin-orbital fluid [7,8], orbital glass [9], the coexistence of ferromagnetism and ferroelectricity [10–12], the so-called Jahn–Teller effect [13–15], and phenomena attributed to the competing exchange of ferromagnetism (FM) and anti-ferromagnetism (AFM) of almost equal strength, causing a strong bond frustration [16].

Many interesting properties were observed in the spinel series that fulfil Vegard's law in the full-concentration region. In the Katowice group at the end of the 20th century, the $\text{Zn}_{1-x}\text{Cu}_x\text{Cr}_2\text{Se}_4$ spinel series was particularly intensively studied, the edge spinels of which ZnCr_2Se_4 and CuCr_2Se_4 were respectively antiferromagnet and ferromagnet, and at the same time, a semiconductor and a conductor [17–19]. In the early 2000s, Parker et al. [20] discovered a transition from positive to negative magnetoresistance there.

Single crystals are used in modern, innovative technology and the electronic industry. The semiconducting [21] and antiferromagnetic [22] ZnCr_2Se_4 spinel is a matrix for various diluted systems where the effects of the site disorder, lattice frustration, and

random distribution of spin interactions [23] create novel potential applications in spin-based electronic technology. In ZnCr_2Se_4 , the spin order occurring at the Néel temperature $T_N = 21$ K [1] is an incommensurate spiral due to the narrow distances between Cr ions. Still, the larger ones cause ferromagnetic (FM) interactions confirmed by the positive Curie–Weiss temperature of $\theta = 90$ K [21,22]. For this reason, differences in magnetic interactions between the nearest and farther neighbours in ZnCr_2Se_4 are related to the frustration of chemical bonds that play an essential role. The magnetic order is accompanied by structural transformation from cubic $Fd\bar{3}m$ to tetragonal $I4_1/amd$ symmetry with a slight contraction along the c axis [24,25], manifested by sharp first-order anomalies at T_N on the specific heat curve [1].

Our group's work has been done based on the ZnCr_2Se_4 matrix. This matrix has been doped with both non-magnetic ions, such as, for example, Al [26–28], Cu [17–19,29,30], Ga [17,18,31–33], In [18,33,34], Sn [35,36], and Ta [37], and with magnetic ones, such as, for example, Dy [38,39], Gd [40], Ho [41], Mn [42,43], Nd [44], and Ni [45]. All the above-mentioned doped spinels have two features in common. They are semiconductors and antiferromagnets, just like a matrix. An interesting feature is the appearance of the re-entrant-type spin-glass when non-magnetic Al [27] and Sn [36] ions are located in the octahedral sites of the spinel structure. It was also observed that Sn ions occupying octahedral sites reduce the n -type electrical conductivity by magnitude compared to samples in which they occupy tetrahedral ones [35]. This interesting phenomenon has been explained based on the quantum band model, which predicts a lowering of the Fermi level in the lowest Cr^{3+} Mott–Hubbard sub-band with a narrowed $3d^3 t_{2g}$ band, which gives an increase in the energy gap when Sn^{3+} ions (spin defects) are replaced at octahedral sites instead of Cr^{3+} ones [35]. Interestingly, geometric spin-glass was observed when substituting Dy ions, a paramagnetic rare-earth ion in both tetrahedral and octahedral positions [39].

This work continues our research that involved introducing the p-block element into the crystal lattice ZnCr_2Se_4 . Pb belongs to group 14 of the periodic table. Sn also belongs to this group. ZnCr_2Se_4 single crystals doped with tin showed the phenomenon of spin-glass [36]. It was assumed that the presence of Pb ions in the ZnCr_2Se_4 crystal lattice would affect the physicochemical properties of the parent compound. A single crystal growth model was developed using a computer programme. The structural, magnetic, electrical, and thermal properties were determined using various methods (XRD—X-ray Diffraction, SEM—Scanning Electron Microscopy, DSC—Differential Scanning Calorimetry, TG—Thermogravimetry, SQUID—Superconducting Quantum Interference Device, QD-PPMS—Quantum Design Physical Property Measurement System). This work presents the structural, magnetic, electrical, thermal, and specific heat properties of five monocrystalline samples doped with diamagnetic Pb^{2+} ions with a large ion radius instead of Zn^{2+} ones. The novelty of this work is the study of the ac magnetic susceptibility measured in an external dc magnetic field up to 50 kOe. According to our knowledge, such crystals have not been described in the literature.

2. Materials and Methods

High-purity elements, Zn, Pb, Cr, Se (5N, Sigma Aldrich, Sofia, Bulgaria), and anhydrous CrCl_3 (Sigma Aldrich), were applied to synthesise ZnCr_2Se_4 single crystals doped with Pb.

2.1. Computation of Thermodynamic Parameters for the Chemical Transport Reactions

The basis for the growth of single crystals by gaseous chemical transport is reversible transport reactions. The criterion determining the reaction's transport capacity is the order of magnitude of the equilibrium constant K_p . The K_p value should be close to 1 ($\log K_p \approx 0$). The following dependence is used to assess the transport capacity of the reaction:

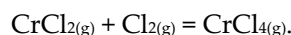
$$\Delta G_T^0 = \Delta H_{298K}^0 - T\Delta S_{298K}^0 \quad (1)$$

where ΔH_{298K}^0 and ΔS_{298K}^0 are the corresponding changes of the reaction's standard and enthalpy and entropy. Free energy variations can be used to assess the transportability of the reaction ΔG^0 instead of the equilibrium constant K_p because these quantities are related to the formula:

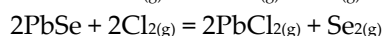
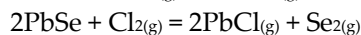
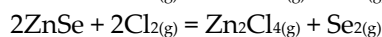
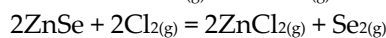
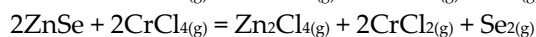
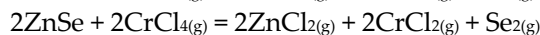
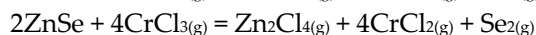
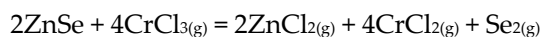
$$\Delta G^0 = -2.303RT \log K_p = \Delta H^0 - T\Delta S^0, \quad (2)$$

where: R —gas constant; T —absolute temperature; K_p —equilibrium constant; ΔG^0 , ΔH^0 , ΔS^0 —changes in the reaction's free energy, enthalpy, and entropy. Accompanying reactions related to the solvent or reaction products' dissociation may occur during the transport process. Therefore, all independent reactions occurring in the tested system should be considered. The selection of an appropriate transport substance involves finding such transport reactions for which the values of K_p or ΔG^0 , in the selected temperature range, do not deviate too much from the equilibrium values. We are looking for a substance that will produce sizeable partial pressure differences Δp_i , with the slightest possible temperature difference.

In the process of selenium chromite single crystal growth, anhydrous CrCl_3 is used, which dissociates at a temperature above 773 K according to the following reactions [46,47]:



In a closed system, in a gas solution, apart from CrCl_3 and Cl_2 , there is also CrCl_4 . Therefore, the dissociation products should be taken into account when creating a set of all independent transport reactions that occur simultaneously in the ZnSe-PbSe-CrCl_3 system:



These hypothetical reactions were used to calculate the temperature dependence of the thermodynamic parameters (ΔH^0 , ΔG^0 , ΔS^0 , and $\log K_p$). The calculations were performed using the H.S.C. Chemistry 6 computer programme. Based on these calculations, the reaction conditions (dissolution zone temperatures and crystallisation and their difference (Table 1)) make it possible to obtain good-quality crystals.

Table 1. Conditions of growth and chemical composition of ZnCr₂Se₄:Pb single crystals.

| № | Amounts of Substrates (mmol) | | T_d (K) | T_c (K) | ΔT (K) | % Weight | | | | Chemical Formula |
|-----|------------------------------|-------|-----------|-----------|----------------|--------------|-------------|--------------|--------------|---|
| | nZnSe | nPbSe | | | | Zn | Pb | Cr | Se | |
| (1) | 14.4 | 1.6 | 1223 | 1163 | 60 | 12.31 ± 0.09 | 3.23 ± 0.06 | 20.66 ± 0.01 | 63.71 ± 0.04 | Zn _{0.94} Pb _{0.06} Cr ₂ Se ₄ |
| (2) | 14.4 | 1.6 | 1133 | 1083 | 50 | 12.25 ± 0.08 | 2.95 ± 0.07 | 20.45 ± 0.02 | 64.54 ± 0.05 | Zn _{0.92} Pb _{0.07} Cr ₂ Se ₄ |
| (3) | 12.8 | 3.2 | 1203 | 1153 | 50 | 12.05 ± 0.06 | 3.43 ± 0.06 | 20.49 ± 0.05 | 64.10 ± 0.03 | Zn _{0.92} Pb _{0.09} Cr ₂ Se ₄ |
| (4) | 12.8 | 3.2 | 1203 | 1143 | 60 | 11.63 ± 0.02 | 4.51 ± 0.04 | 20.30 ± 0.06 | 63.56 ± 0.03 | Zn _{0.89} Pb _{0.11} Cr ₂ Se ₄ |
| (5) | 11.2 | 4.8 | 1203 | 1153 | 50 | 11.42 ± 0.03 | 4.98 ± 0.05 | 20.15 ± 0.03 | 63.42 ± 0.03 | Zn _{0.88} Pb _{0.12} Cr ₂ Se ₄ |

Chemical compositions were determined using Scanning Electron Microscopy. T_d is the temperature of the dissolution zone, T_c is the temperature of the crystallisation zone, and ΔT is the difference in temperatures between the dissolution and the crystallisation zones.

2.2. Synthesis of ZnSe and PbSe

The polycrystalline ZnSe and PbSe were obtained by the high-temperature sintering of powders (1073 K) using a solid-state reaction in a high vacuum (10^{-5} mbarr).

2.3. Crystal Structure and Chemical Composition

The X-ray diffraction measurement was carried out at 293(1) K. Five samples with different nominal Pb content were selected under a stereoscopic Zeiss optical microscope. A small crystal (diameter of about 0.1 mm) was mounted on a glass capillary. The data were collected using a SuperNova X-ray diffractometer with a microfocus X-ray tube, optimised multi-layer optics for Mo-K α ($\lambda = 0.71073$ Å) radiation, and an Atlas CCD detector. Accurate cell parameters were determined and refined with CrysAlisPro software (Version 1.171.37.35, Agilent Technologies, Wrocław, Poland, 2014). Moreover, the CrysAlisPro program was used to integrate the collected data. The spinel structure (space group no. 227) was refined using the SHELXL-2013 program [48]. All atoms were refined with anisotropic displacement parameters. The chemical composition of the single crystals was studied using a Scanning Electron Microscope JEM 6480 equipped with an energy-dispersive X-ray spectrometer (SEM/EDS). The solid elements (Zn, Pb, Cr, Se) were used as standards to determine the mass % content of the elements in the sample. Measurements were carried out at 20 locations of the single crystal to determine the average chemical composition. Each of the measuring areas was approximately 50×30 μm . Then, the average chemical composition was calculated, which is shown in Table 1. The error bar represents the standard deviation. Relatively low values of the standard deviation indicate good homogeneity of the chemical composition.

2.4. Magnetic and Electrical Measurements

Dynamic ac magnetic susceptibility, χ_{ac} , was measured in the temperature range 2–300 K and at an internal oscillating magnetic field $H_{ac} = 1$ Oe, with an internal frequency $f = 120$ Hz taken at external static dc magnetic fields $H_{dc} = 0, 10, 20, 30, 40$, and 50 kOe. Magnetisation isotherms, $M(H)$, were measured at 2, 10, 20, 40, 60, and 300 K and in the static magnetic field up to 70 kOe. A Quantum Design MPMS-XL-7AC SQUID magnetometer (Quantum Design, San Diego, CA, U.S.A.) was used. The Néel (T_N) and T_m temperatures and the critical fields were defined as the extremes corresponding to the derivative of $d\chi_{ac}/dT$ vs. T and dM/dH vs. H . The effective magnetic moment was calculated using the equation [37,42,49]: $\mu_{eff} = 2.828\sqrt{C}$, where C is the Curie constant. The magnetic super-exchange integrals for the first two coordination spheres, J_1 and J_2 , were calculated using the Holland and Brown equations [50]: $J_1 = (-9T_N + \theta)/60$ and $J_2 = (3T_N + \theta)/120$. The electrical conductivity, $\sigma(T)$, was measured by the dc method using a KEITHLEY 6517B Electrometer/High Resistance Meter (Keithley Instruments, L.L.C.,

Solon, OH, USA) in the temperature range of 77–400 K. The activation energy, E_a , was determined below room temperature and in the temperature range of 300–400 K from the formula $\sigma = \sigma_0 \exp(-\frac{E_a}{kT})$, where k is the Boltzmann constant and σ_0 is the reference conductivity. The details of methods used to determine the electrical properties, thermal analysis, and specific heat are described in [37,39,41,44].

3. Results and Discussion

3.1. Growth of Single Crystals and Chemical Composition

Thermodynamic calculations indicate that, for the ZnSe–PbSe–CrCl₃ system, the simultaneous transport of ZnSe and PbSe will be realised using gaseous CrCl₃ and CrCl₄ ($\log K_p$ and ΔG^0 values are close to zero in the selected temperature range: 1000–1400 K). It is shown in Figures 1 and 2 that, for chemical reactions with CrCl₃ and CrCl₄, the enthalpy values are positive ($\Delta H^0 > 0$), which indicates that the transport takes place from a higher temperature to a lower temperature in the direction of the formation of products.

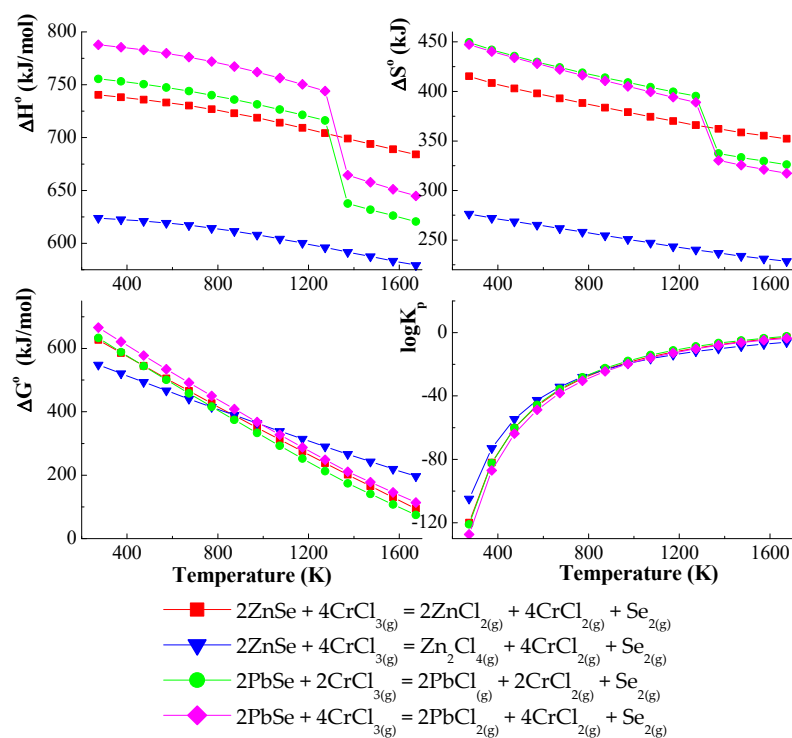


Figure 1. The dependence of the thermodynamic parameters vs. temperature T for the ZnSe and PbSe with CrCl₃ as a transport agent.

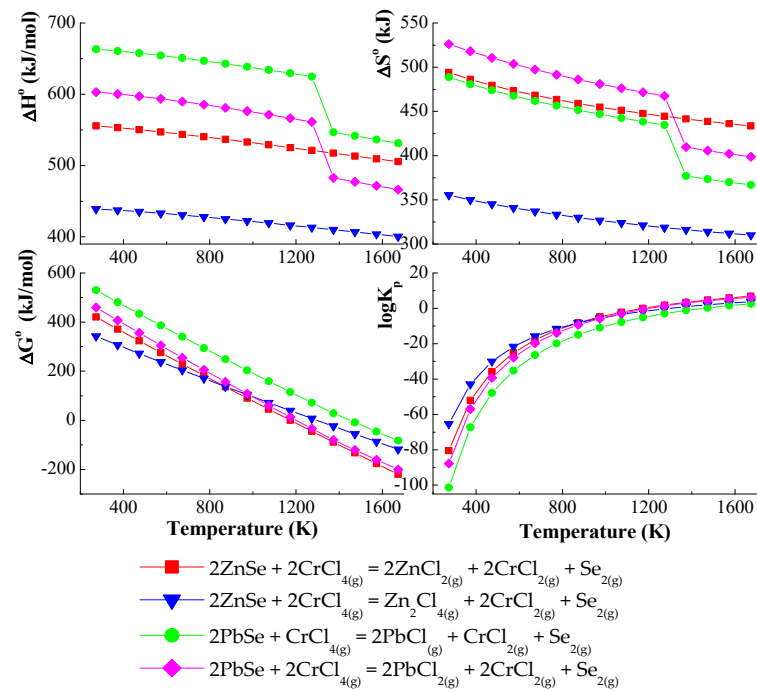


Figure 2. The dependence of the thermodynamic parameters vs. temperature T for the ZnSe and PbSe with CrCl_4 as a transport agent.

On the other hand, the enthalpy values for the transport of reactions with chlorine (Cl_2) are negative ($\Delta H^\circ < 0$), which indicates that the reaction equilibrium is shifted towards the reactants. Based on these calculations, it has been confirmed that in the ZnSe–PbSe– CrCl_3 system, ZnSe and PbSe are mainly transported by gaseous CrCl_3 and CrCl_4 . Values of $\log K_p$ are close to zero in the selected temperature range: 1000–1400 K (Figure 3).

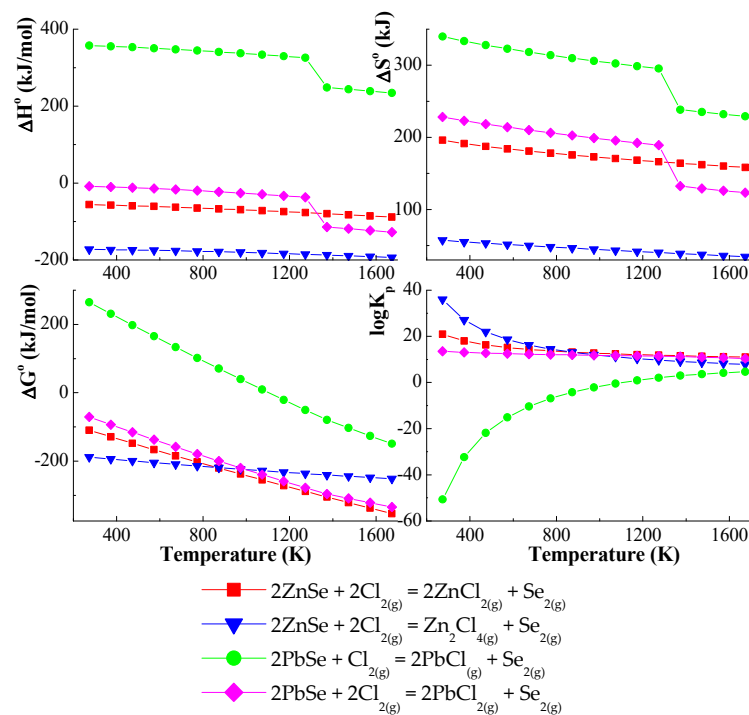
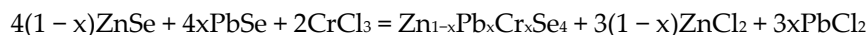


Figure 3. The dependence of the thermodynamic parameters vs. temperature T for the ZnSe and PbSe with Cl_2 as a transport agent.

Synthesis of single crystals of $\text{Zn}_{1-x}\text{Pb}_x\text{Cr}_2\text{Se}_4$ was carried out according to the reaction:



for $x = 0.1, 0.2, 0.3$.

Thermodynamic calculations determined the reaction conditions, such as dissolution and crystallisation temperatures, and their difference. The crystallisation zone temperature was between 1083 and 1153 K. The dissolution zone was between 1133 and 1233 K. Their difference was 50–70 K. Based on our experience with the growth of doped ZnCr_2Se_4 single crystals, we can state that a minor temperature difference (ΔT) is more favourable for crystal growth. Stoichiometric mixtures of the ZnSe , PbSe , and CrCl_3 were introduced to quartz ampoules (length—200 mm, inner diameter—20 mm) evacuated to 10^{-5} mbarr. The sealed ampoules were placed in a two-zone tubular furnace and heated for 450 h. After heating, the ampoules were cooled at about 70 degrees per hour. Such a preparation process for the growth of single crystals allowed for obtaining single crystals of good quality (Figure 4). Five single crystals with various Pb content were chosen for X-ray diffraction measurements. The reaction conditions and results of SEM analysis, together with determined chemical formulae, are shown in Table 1.

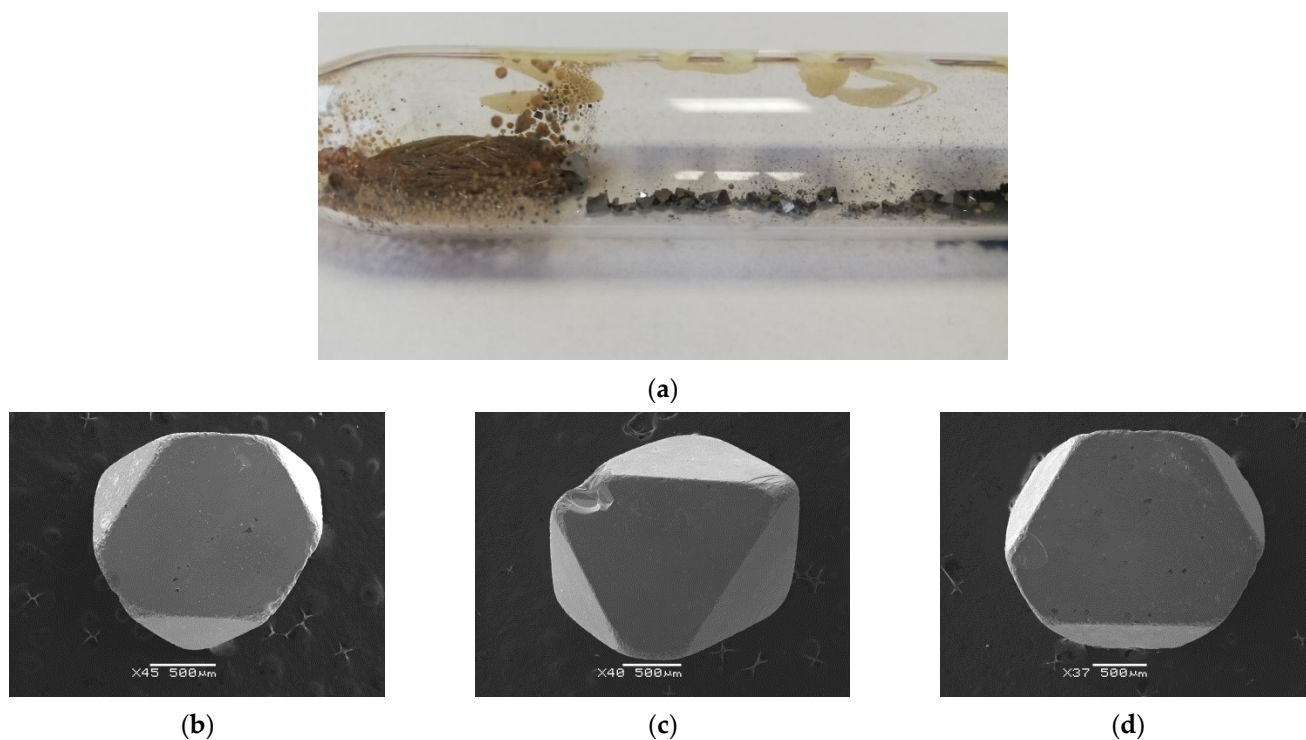


Figure 4. (a) A part of quartz ampoule with obtained $\text{ZnCr}_2\text{Se}_4\text{:Pb}$ single crystals. Examples of single crystals obtained in the $\text{ZnCr}_2\text{Se}_4\text{:Pb}$ system: (b) $\text{Zn}_{0.94}\text{Pb}_{0.06}\text{Cr}_2\text{Se}_4$, (c) $\text{Zn}_{0.92}\text{Pb}_{0.09}\text{Cr}_2\text{Se}_4$, (d) $\text{Zn}_{0.88}\text{Pb}_{0.12}\text{Cr}_2\text{Se}_4$.

3.2. Structural Study

Based on the structure of ZnCr_2Se_4 , in which the Zn^{2+} ions occupy the tetrahedral position 8a: $1/8, 1/8, 1/8$ (A-site), and the Cr^{3+} ions occupy the position 16d: $1/2, 1/2, 1/2$ (B-site), according to the spinel structure, we considered two models of cation distribution. In the first model, the presence of Pb^{2+} ions in A-sites was assumed with coupled site occupancy factors (SOF) and constrained atomic displacements. The second model assumed that the Pb^{2+} ions would substitute the Cr^{3+} ones. Because of the strong correlation, the SOFs for Cr and Pb were refined separately in alternative calculations. The as-

sumed oxidation state of Pb and the correlations of the refined parameters caused the rejection of the second model.

Based on this refinement, the first model allowed us to obtain the acceptable atomic displacement parameters and SOFs. We could describe the general chemical formula for obtained single crystals as presented in Tables 2 and 3. The observed slight increase in thermal shift at the A-site points out a static disturbance in the location of the $\text{Zn}^{2+}/\text{Pb}^{2+}$ pseudo-ion, which is usually caused by the difference in ionic charges and in ionic and covalent radii ($r_i(\text{Zn}^{2+}) = 0.60 \text{ \AA}$, $r_i(\text{Cr}^{3+}) = 0.62 \text{ \AA}$, $r_i(\text{Pb}^{2+}) = 0.98 \text{ \AA}$ and $R_c(\text{Zn}^{2+}) = 0.74 \text{ \AA}$, $R_c(\text{Cr}^{3+}) = 0.76 \text{ \AA}$, $R_c(\text{Pb}^{2+}) = 1.12 \text{ \AA}$, respectively) [51].

Table 2. Structural parameters of the $\text{Zn}_{1-x}\text{Pb}_x\text{Cr}_2\text{Se}_4$ single crystals.

| Chemical Formula | Lattice Parameter (\AA) | Volume (\AA^3) | Density Calc. (Mg/m^3) | Absorption Coeff. (mm^{-1}) | Goodness of R Parameters | | |
|--|------------------------------------|---------------------------|-----------------------------------|--|--------------------------|--------|--------|
| | | | | | Fit on F^2 | R_1 | wR_2 |
| $\text{Zn}_{0.94}\text{Pb}_{0.06}\text{Cr}_2\text{Se}_4$ | 10.4910(3) | 1154.65(2) | 5.682 | 32.837 | 1.150 | 0.0223 | 0.0662 |
| $\text{Zn}_{0.92}\text{Pb}_{0.07}\text{Cr}_2\text{Se}_4$ | 10.4933(2) | 1155.41(3) | 5.689 | 32.883 | 1.205 | 0.0333 | 0.1114 |
| $\text{Zn}_{0.92}\text{Pb}_{0.09}\text{Cr}_2\text{Se}_4$ | 10.4946(4) | 1155.84(1) | 5.709 | 32.856 | 1.175 | 0.0261 | 0.0839 |
| $\text{Zn}_{0.89}\text{Pb}_{0.11}\text{Cr}_2\text{Se}_4$ | 10.4954(2) | 1156.10(2) | 5.757 | 33.841 | 1.196 | 0.0333 | 0.1114 |
| $\text{Zn}_{0.88}\text{Pb}_{0.12}\text{Cr}_2\text{Se}_4$ | 10.4959(1) | 1156.27(3) | 5.772 | 33.852 | 1.191 | 0.0311 | 0.1012 |

Table 3. Atomic coordinates and equivalent isotropic displacement parameters of the $\text{Zn}_{1-x}\text{Pb}_x\text{Cr}_2\text{Se}_4$ single crystals. The Wyckoff positions of the atoms in the spinel structure are: Zn in $8b$ ($3/8, 3/8, 3/8$); Cr/Ta in $16c$ ($1/2, 1/2, 1/2$); and Se in $32e$ (x, x, x). U (eq) is defined as one-third of the orthogonalized U_{ij} tensor trace.

| Spinel | Anion Parameter u | Site Occupation | | $U_{\text{iso}} (\text{\AA}^2 \times 10^3)$ | | |
|--|---------------------|-----------------|-----|---|------|------|
| | | (A) | (B) | Zn/Pb | Cr | Se |
| $(\text{Zn}_{0.94}\text{Pb}_{0.06})[\text{Cr}_2]\text{Se}_4$ | 0.2595(1) | 0.94(1):0.06(1) | 1.0 | 13(1) | 7(1) | 7(1) |
| $(\text{Zn}_{0.92}\text{Pb}_{0.07})[\text{Cr}_2]\text{Se}_4$ | 0.2595(1) | 0.92(2):0.07(1) | 1.0 | 14(1) | 6(1) | 6(1) |
| $(\text{Zn}_{0.92}\text{Pb}_{0.09})[\text{Cr}_2]\text{Se}_4$ | 0.2595(1) | 0.92(1):0.09(1) | 1.0 | 13(1) | 7(1) | 6(1) |
| $(\text{Zn}_{0.89}\text{Pb}_{0.11})[\text{Cr}_2]\text{Se}_4$ | 0.2595(1) | 0.89(2):0.11(2) | 1.0 | 14(1) | 5(1) | 5(1) |
| $(\text{Zn}_{0.88}\text{Pb}_{0.12})[\text{Cr}_2]\text{Se}_4$ | 0.2595(1) | 0.87(1):0.13(2) | 1.0 | 14(1) | 5(1) | 6(1) |

The structural study confirmed the chemical composition obtained from SEM. The general formula of obtained single crystals can be described as $\text{Zn}_{1-x}\text{Pb}_x\text{Cr}_2\text{Se}_4$. The Pb ions substituted the Zn ones. The single crystals crystallised in a cubic system with space group $Fd-3m$ (No. 227, $Z = 8$). The lattice parameters of the obtained single crystals are slightly larger than pure ZnCr_2Se_4 ($a = 10.489 \text{ \AA}$) and enhanced with the increase in lead content (Table 2). The increase in lattice parameters is connected with the difference in ionic radii between Zn^{2+} and Pb^{2+} (Figure 5).

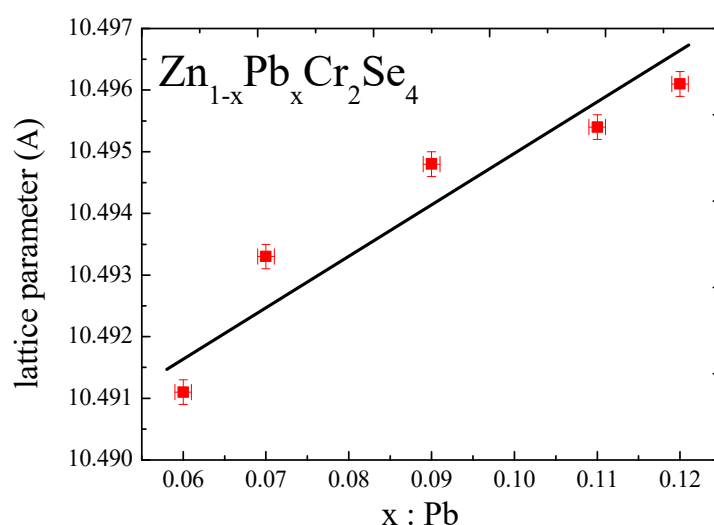


Figure 5. Dependence of the lattice parameters of $\text{Zn}_{1-x}\text{Pb}_x\text{Cr}_2\text{Se}_4$ single crystals on the Pb amount.

The positional parameter of Se (u) is a measure of the anion sublattice distortion from the cubic-close packing. The value of u is the same for all obtained single crystals. Its value increases slightly compared to the ideal value of $u = 0.250$ (Table 3). The admixture of lead does not significantly affect the u -value. The same is observed in the metal–metal and metal–selenium distances (Table 4), where the differences are insignificant [22]. The structure refinement parameters, the selected bond distances, and angles are shown in Tables 3 and 4.

Table 4. Selected interatomic distances (Å) and bond angles (deg) of the $\text{Zn}_{1-x}\text{Pb}_x\text{Cr}_2\text{Se}_4$ spinel single crystals.

| Spinel | Bond Distances | | Bond Angles | |
|--|----------------|-----------|---------------------|---|
| | Zn/Pb–Se | Cr–Se | Se–Zn/Pb–Se | Se–Cr–Se |
| $(\text{Zn}_{0.94}\text{Pb}_{0.06})[\text{Cr}_2]\text{Se}_4$ | 2.4451(5) | 2.5282(3) | $109.5(0) \times 6$ | $180.0(0) \times 3$ $94.61(13) \times 6$ $85.39(13) \times 6$ |
| $(\text{Zn}_{0.92}\text{Pb}_{0.07})[\text{Cr}_2]\text{Se}_4$ | 2.4442(7) | 2.5269(4) | $109.5(0) \times 6$ | $180.0(0) \times 3$ $94.61(2) \times 6$ $85.39(2) \times 6$ |
| $(\text{Zn}_{0.92}\text{Pb}_{0.09})[\text{Cr}_2]\text{Se}_4$ | 2.4453(5) | 2.5274(3) | $109.5(0) \times 6$ | $180.0(0) \times 3$ $94.62(14) \times 6$ $85.38(14) \times 6$ |
| $(\text{Zn}_{0.89}\text{Pb}_{0.11})[\text{Cr}_2]\text{Se}_4$ | 2.4453(8) | 2.5279(4) | $109.5(0) \times 6$ | $180.0(0) \times 3$ $94.62(2) \times 6$ $82.38(2) \times 6$ |
| $(\text{Zn}_{0.88}\text{Pb}_{0.12})[\text{Cr}_2]\text{Se}_4$ | 2.4453(7) | 2.5280(4) | $109.5(0) \times 6$ | $180.0(0) \times 3$ $94.61(2) \times 6$ $85.39(2) \times 6$ |

3.3. Electrical and Magnetic Properties

The results of the electrical measurements are shown in Figure 6 and Table 5, and the magnetic ones are in Figures 7–9 and Tables 5 and 6. Electrical conductivity measurements (Figure 6) showed semiconducting properties in the temperature range of 77–400 K for all single crystals under study. Two regions of Arrhenius type electrical conductivity are visible: the extrinsic one with the activation energy of $E_a \sim 0.08$ eV below

room temperature, independent of the Pb content in the sample, and the intrinsic one with E_a increasing in the range of 0.138–0.315 eV above room temperature with increasing Pb content (Table 5).

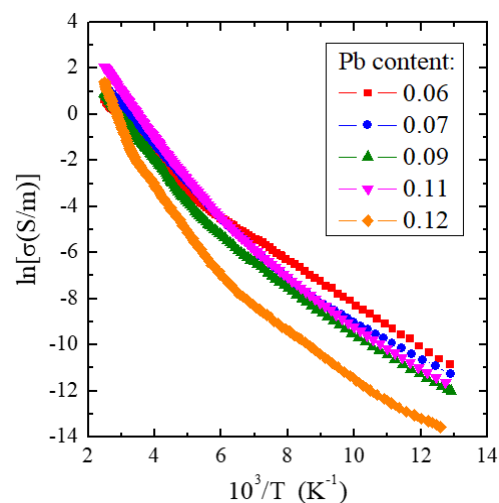
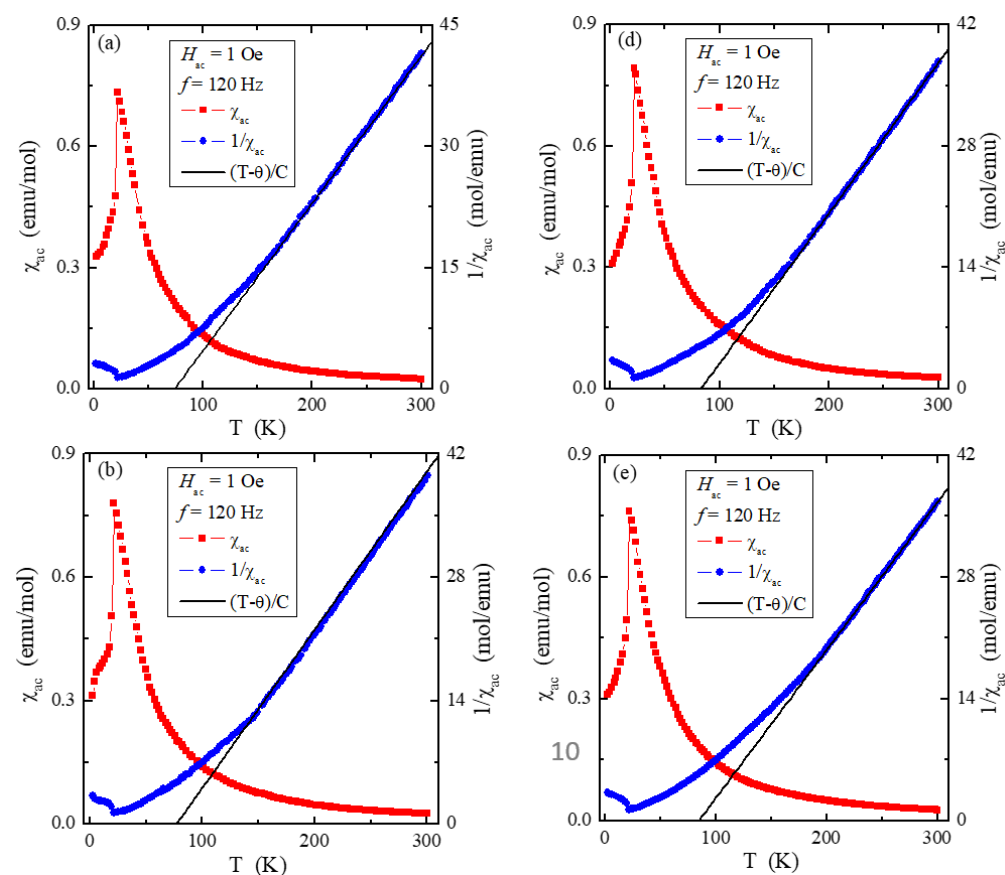


Figure 6. Electrical conductivity ($\ln\sigma$) vs. reciprocal temperature ($10^3/T$) for ZnCr_2Se_4 single crystals doped with Pb^{2+} ions having contents of 0.06, 0.07, 0.09, 0.11, and 0.12.



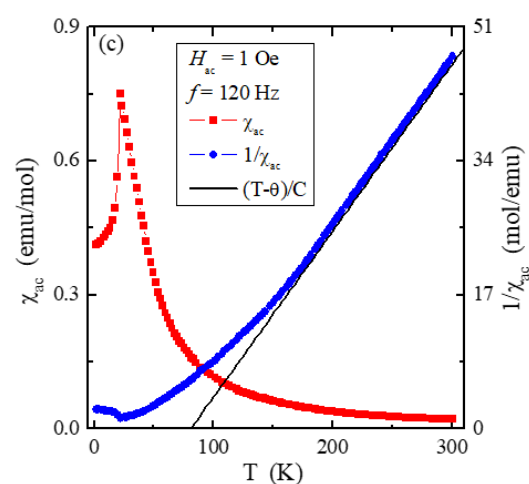


Figure 7. Ac magnetic susceptibility χ_{ac} and its reciprocal $1/\chi_{ac}$ vs. temperature T recorded at internal oscillating magnetic field $H_{ac} = 1$ Oe with internal frequency $f = 120$ Hz for the ZnCr_2Se_4 single crystals doped with Pb^{2+} ions having contents of 0.06 (a), 0.07 (b), 0.09 (c), 0.11 (d), and 0.12 (e). The solid (black) line, $(T-\theta)/C$, indicates a Curie–Weiss behaviour.

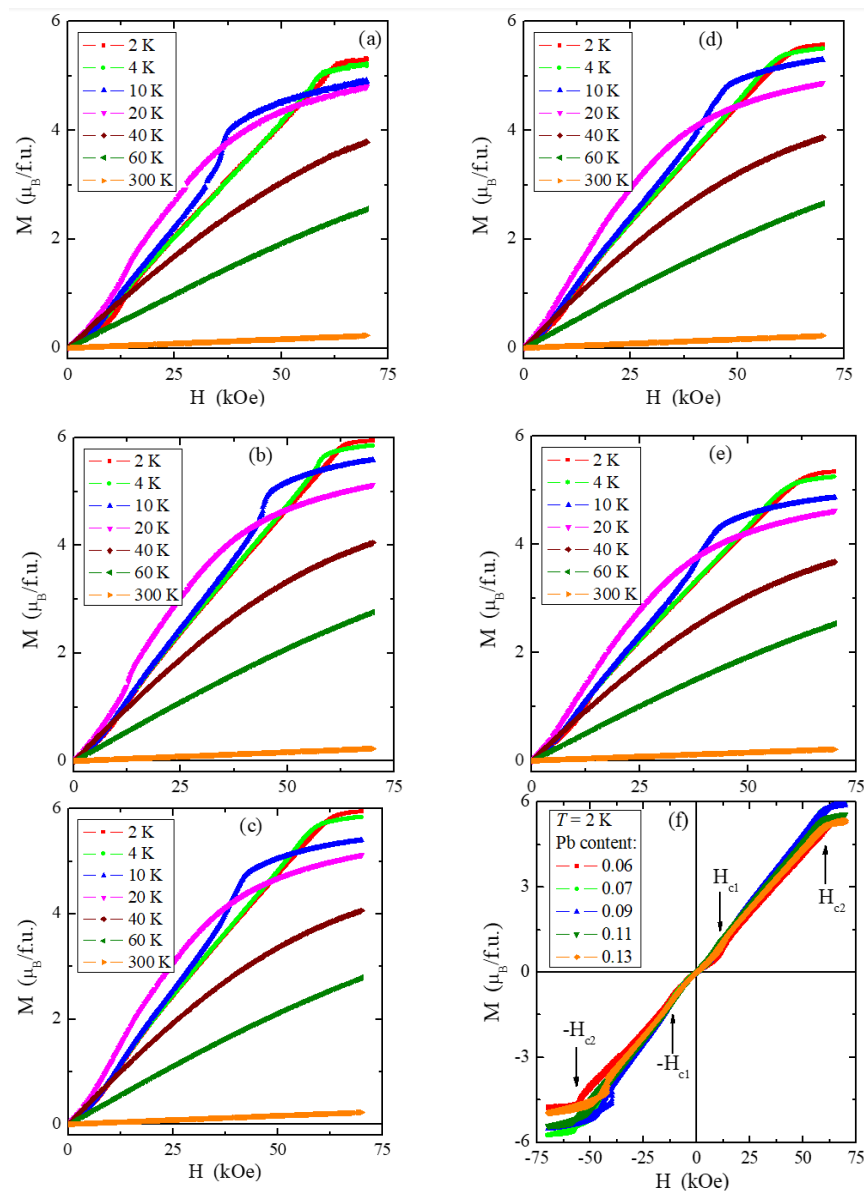


Figure 8. Magnetization M vs. magnetic field H at 2, 4, 10, 20, 40, 60, and 300 K for the ZnCr_2Se_4 single crystals doped with Pb^{2+} ions having contents of 0.06 (a), 0.07 (b), 0.09 (c), 0.11 (d), and 0.12 (e). The $M(H)$ isotherms recorded at 2 K with arrows denoting the first (H_{c1}) and second (H_{c2}) critical magnetic fields are shown in Figure (f).

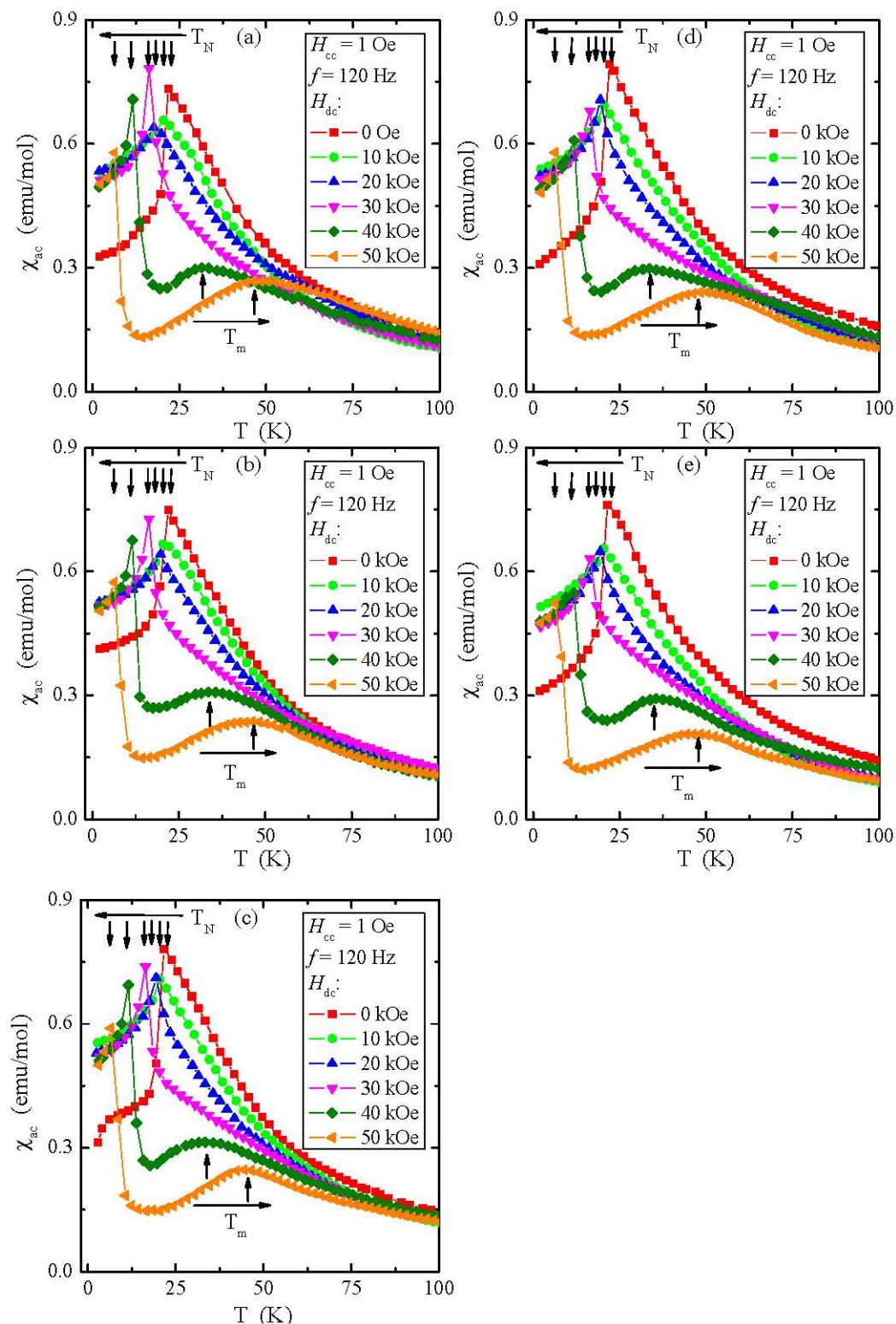


Figure 9. Ac magnetic susceptibility χ_{ac} vs. temperature T recorded at internal oscillating magnetic field $H_{ac} = 1$ Oe with internal frequency $f = 120$ Hz for the ZnCr_2Se_4 single crystals doped with Pb^{2+} ions having contents of 0.06 (a), 0.07 (b), 0.09 (c), 0.11 (d), and 0.12 (e) taken at external magnetic

fields $H_{dc} = 0, 10, 20, 30, 40$, and 50 kOe. Vertical arrows indicate the Néel T_N and T_m temperatures, and horizontal ones indicate the shift of T_N and T_m with increasing magnetic field H_{dc} .

Table 5. Magnetic parameters of $Zn_{1-x}Pb_xCr_2Se_4$ single crystals recorded in an internal oscillating magnetic field $H_{ac} = 1$ Oe with an internal frequency $f = 120$ Hz and with a zero external static magnetic field: C is the Curie constant; T_N and θ are the Néel and Curie–Weiss temperatures, respectively; μ_{eff} is the effective magnetic moment; J_1 and J_2 are the super-exchange integrals for the first two coordination spheres. H_{c1} and H_{c2} are the critical fields measured at the static magnetic field up to 70 kOe. E_a is the energy activation measured in the temperature range of 300 – 400 K. Experimental data for the $ZnCr_2Se_4$ matrix were taken from Refs. [1,21,22,31] for comparison.

| Spinel | C (emu·K/mol) | T_N (K) | θ (K) | μ_{eff} ($\mu_B/f.u.$) | $M_{s(2K)}$ ($\mu_B/f.u.$) | J_1 (K) | J_2 (K) | H_{c1} (kOe) | H_{c2} (kOe) | E_a (eV) |
|------------------------------|------------------|--------------|-----------------|---------------------------------|---------------------------------|--------------|--------------|-------------------|-------------------|---------------|
| $ZnCr_2Se_4$ | 4.082 | 21 | 90 | 5.714 | 6.0 | −1.65 | 1.28 | 10.0 | 65.0 | 0.135 |
| $Zn_{0.94}Pb_{0.06}Cr_2Se_4$ | 5.477 | 22 | 74 | 6.618 | 5.325 | −2.07 | 1.17 | 12.0 | 55.0 | 0.138 |
| $Zn_{0.92}Pb_{0.07}Cr_2Se_4$ | 5.568 | 22 | 77 | 6.673 | 5.964 | −1.95 | 1.23 | 12.0 | 56.0 | 0.161 |
| $Zn_{0.92}Pb_{0.09}Cr_2Se_4$ | 4.727 | 22 | 81 | 6.149 | 5.960 | −2.02 | 1.19 | 12.0 | 61.0 | 0.146 |
| $Zn_{0.89}Pb_{0.11}Cr_2Se_4$ | 5.768 | 22 | 83 | 6.792 | 5.486 | −1.92 | 1.24 | 12.0 | 55.0 | 0.177 |
| $Zn_{0.88}Pb_{0.12}Cr_2Se_4$ | 5.898 | 22 | 84 | 6.868 | 5.251 | −1.90 | 1.25 | 12.0 | 57.0 | 0.315 |

The increase in activation energy with the increase in lead content may be caused by the appearance of cationic vacancies (acting as double acceptors) because the radius of Pb^{2+} ions is much larger than that of Zn^{2+} ones [51]. It may result in acceptor vacancy levels in the energy gap. The activation energies mentioned above correlate well with E_a for the matrix [31] and with its admixtures, such as tin [35], tantalum [37], and dysprosium [22].

The temperature dependencies of ac magnetic susceptibility χ_{ac} , recorded in an internal oscillating magnetic field $H_{ac} = 1$ Oe with an internal frequency $f = 120$ Hz and with a zero external static magnetic field (Figure 7a–e), show AFM order with the Néel temperature $T_N = 22$ K and the positive Curie–Weiss temperature (θ) slightly changing from 74 K to 84 K as the Pb content increases (Table 5).

The θ values are much lower than the literature data published in [21,22] and slightly lower than in [1], where θ is equal to 115 K and 90 K, respectively. Thus, only the T_N temperature values are close to this temperature's values for the $ZnCr_2Se_4$ matrix [1,21,22]. It means that the long-range AFM interactions are slightly more substantial. In contrast, the short-range FM ones are somewhat weaker in the sample containing Pb, which is confirmed by both the long bond lengths (Table 4) and the values of the J_1 and J_2 super-exchange integrals for the first two coordination spheres (Table 5). A significant difference was observed between the effective magnetic moment (μ_{eff}) and the effective number of Bohr magnetons, $p_{eff} = 5.477$, i.e., the spin contribution to the magnetic moment for Cr^{3+} ions per molecule $3d^3$ configuration. It may suggest that the orbital magnetic contribution has not been quenched at low amplitude, $H_{ac} = 1$ Oe, of the applied oscillating magnetic field.

The magnetisation measurements (Figure 8a–e) show that the magnetic saturation of the studied samples is close to the value of $6 \mu_B/f.u.$ for the matrix; the first critical field is kept constant at $H_{c1} = 12$ kOe, and the second critical field is around $H_{c2} = 57$ kOe (Table 5). The hysteresis loops have zero-field coercivity and zero remanences (Figure 8f).

The temperature dependencies of ac magnetic susceptibility χ_{ac} , recorded in an internal oscillating magnetic field $H_{ac} = 1$ Oe with an internal frequency $f = 120$ Hz and taken at external static magnetic fields $H_{dc} = 0, 10, 20, 30, 40$, and 50 kOe, are shown in Figure 9a–e. With the increase in H_{dc} , we observed a shift of T_N towards lower temperatures and of θ towards higher ones (Table 6).

Table 6. Magnetic parameters of the $\text{Zn}_{1-x}\text{Pb}_x\text{Cr}_2\text{Se}_4$ single crystals recorded in an internal oscillating magnetic field $H_{ac} = 1$ Oe with an internal frequency $f = 120$ Hz and taken at external static magnetic fields $H_{dc} = 0, 10, 20, 30, 40$, and 50 kOe: C is the Curie constant; T_N , θ , and T_m are the Néel, Curie–Weiss, and the spin fluctuation temperatures, respectively; μ_{eff} is the effective magnetic moment; and J_1 and J_2 are the super-exchange integrals for the first two coordination spheres.

| Spinel | H_{dc} (kOe) | C (emu·K/mol) | T_N (K) | θ (K) | T_m (K) | μ_{eff} ($\mu_B/f.u.$) | J_1 (K) | J_2 (K) |
|--|-------------------|--------------------|--------------|-----------------|--------------|---------------------------------|--------------|--------------|
| $\text{Zn}_{0.94}\text{Pb}_{0.06}\text{Cr}_2\text{Se}_4$ | 0 | 5.477 | 22 | 74 | - | 6.618 | −2.07 | 1.17 |
| | 10 | 4.211 | 22 | 76 | - | 5.803 | −1.73 | 1.13 |
| | 20 | 4.086 | 18 | 79 | - | 5.716 | −1.38 | 1.11 |
| | 30 | 3.986 | 16 | 82 | - | 5.646 | −1.03 | 1.08 |
| | 40 | 3.948 | 12 | 95 | 31.5 | 5.619 | 0.22 | 1.09 |
| | 50 | 3.863 | 6 | 108 | 46 | 5.558 | 0.90 | 1.05 |
| $\text{Zn}_{0.92}\text{Pb}_{0.07}\text{Cr}_2\text{Se}_4$ | 0 | 5.568 | 22 | 77 | - | 6.673 | −1.95 | 1.23 |
| | 10 | 4.182 | 20 | 78 | - | 5.783 | −1.6 | 1.18 |
| | 20 | 4.102 | 19 | 81 | - | 5.728 | −1.45 | 1.18 |
| | 30 | 4.003 | 16 | 84 | - | 5.658 | −0.9 | 1.11 |
| | 40 | 3.988 | 12 | 96 | 33 | 5.648 | −0.18 | 1.11 |
| | 50 | 3.976 | 7 | 99 | 44 | 5.639 | 0.60 | 1.00 |
| $\text{Zn}_{0.92}\text{Pb}_{0.09}\text{Cr}_2\text{Se}_4$ | 0 | 4.727 | 22 | 81 | - | 6.149 | −2.02 | 1.19 |
| | 10 | 3.922 | 21 | 82 | - | 5.601 | −1.85 | 1.18 |
| | 20 | 3.711 | 20 | 84 | - | 5.448 | −1.65 | 1.17 |
| | 30 | 3.681 | 16 | 85 | - | 5.426 | −1.00 | 1.10 |
| | 40 | 3.602 | 12 | 97 | 33.5 | 5.367 | −0.20 | 1.10 |
| | 50 | 3.639 | 6 | 108 | 46 | 5.369 | 0.90 | 1.05 |
| $\text{Zn}_{0.89}\text{Pb}_{0.11}\text{Cr}_2\text{Se}_4$ | 0 | 5.768 | 22 | 83 | - | 6.792 | −1.92 | 1.24 |
| | 10 | 4.293 | 20 | 84 | - | 5.859 | −1.60 | 1.20 |
| | 20 | 4.182 | 19 | 85 | - | 5.783 | −1.4 | 1.18 |
| | 30 | 4.101 | 16 | 86 | - | 5.727 | −0.97 | 1.12 |
| | 40 | 4.056 | 12 | 91 | 34 | 5.695 | −0.28 | 1.06 |
| | 50 | 4.002 | 6 | 97 | 48 | 5.657 | 0.72 | 0.96 |
| $\text{Zn}_{0.88}\text{Pb}_{0.12}\text{Cr}_2\text{Se}_4$ | 0 | 5.898 | 22 | 84 | - | 6.868 | −1.90 | 1.25 |
| | 10 | 3.794 | 20 | 86 | - | 5.508 | −1.57 | 1.22 |
| | 20 | 3.781 | 19 | 88 | - | 5.499 | −1.38 | 1.21 |
| | 30 | 3.762 | 16 | 90 | - | 5.485 | −0.90 | 1.15 |
| | 40 | 3.703 | 12 | 94 | 36 | 5.442 | −0.23 | 1.08 |
| | 50 | 3.689 | 6 | 98 | 48 | 5.432 | 0.73 | 0.97 |

A strong magnetic field weakens the AFM order and strengthens the FM one. Moreover, the Curie constant, C , and the effective moment μ_{eff} , are close to the values typical for a chromium ion per molecule. For $H_{dc} = 50$ kOe, the J_1 super-exchange integral for the first coordination sphere changes the sign from negative to positive, while the J_2 integral remains positive (Table 6). It means that the short-range FM interaction extends over the entire temperature range. The $\chi_{ac}(T)$ curves above T_N in the paramagnetic region show characteristic wide maxima at $T_m = 32$ – 36 and 44 – 48 K in the fields $H_{dc} = 40$ and 50 kOe, respectively. These broad maxima of ac magnetic susceptibility may be due to the spin fluctuations that occur due to the amplification of short-range FM interactions by a static magnetic field, which is opposed by the thermal energy kT . Similar maxima were found in the ZnCr_2Se_4 matrix doped with Al [28], Ce, Ga, and In [33].

3.4. Specific Heat Studies

In Figure 10, the points represent the specific heat measured for samples with the formulae: $\text{Zn}_{0.92}\text{Pb}_{0.07}\text{Cr}_2\text{Se}_4$, $\text{Zn}_{0.92}\text{Pb}_{0.09}\text{Cr}_2\text{Se}_4$, $\text{Zn}_{0.89}\text{Pb}_{0.11}\text{Cr}_2\text{Se}_4$, and $\text{Zn}_{0.88}\text{Pb}_{0.12}\text{Cr}_2\text{Se}_4$.

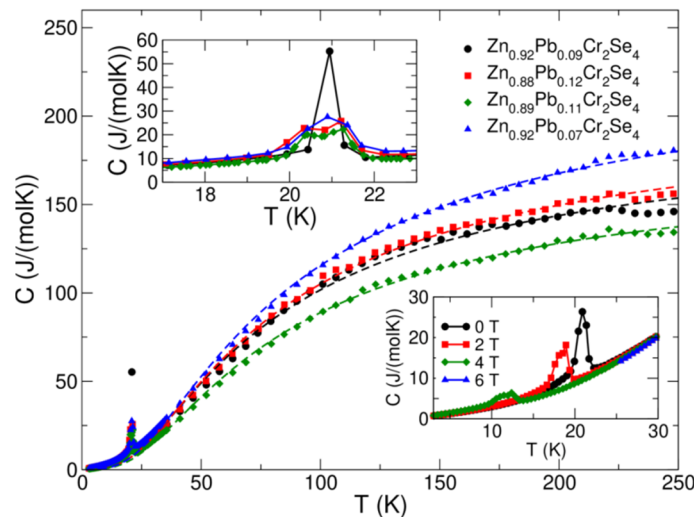


Figure 10. Specific heat, C , as a function of temperature T , measured for the $\text{Zn}_{1-x}\text{Pb}_x\text{Cr}_2\text{Se}_4$ single crystals ($x = 0.07, 0.09, 0.11$, and 0.12) at zero magnetic field (main figure). The dashed lines show the Debye model fit experimental data for $T > 40$ K. The upper inset shows how the magnetic peak is affected by Pb substitution. The lower inset shows how the magnetic transition temperature is affected by the magnetic field for the $\text{Zn}_{0.92}\text{Pb}_{0.07}\text{Cr}_2\text{Se}_4$ sample. Note that the temperature scales on the lower and upper inset are not the same. Hence, the peaks in the upper inset appear much broader than in the lower inset or the main Figure.

We see that the Debye model fits the experimental data well for all the samples, with the Debye temperatures obtained from the fits 163–177 K, with no apparent dependence of Debye temperature on the Pb concentration. The number of atoms obtained from the fit lies within 7.2–9.5 for the investigated samples, without clear dependence on the Pb concentration. It can be explained by the fact that the change in sample composition is minute, and the changes in Zn concentration accompany the changes in Pb concentration. The upper inset of Figure 10 shows the specific heat in a narrow region around the magnetic ordering temperature. The sample $\text{Zn}_{0.92}\text{Pb}_{0.09}\text{Cr}_2\text{Se}_4$ exhibits quite a sharp peak in the vicinity of magnetic transition, whereas the remaining compositions show a broader two-peak-like structure. This is most likely caused by the disorder induced by the Pb substitution and the lack of full site occupancy of the Zn site. The bottom inset of Figure 10 shows the shift of the magnetic transition with the increase in magnetic field for the $\text{Zn}_{0.92}\text{Pb}_{0.07}\text{Cr}_2\text{Se}_4$ sample, which is a clear manifestation of antiferromagnetic order.

We also measured the resistivity for the $\text{Zn}_{0.88}\text{Pb}_{0.12}\text{Cr}_2\text{Se}_4$ sample (the sample with the highest Pb concentration) with the resistivity option in the PPMS instrument (Figure 11). Below 120 K, the resistivity exceeded the range of the instrument. However, in the 120–300 K range, the resistivity can be well-fitted with an activation law $\rho = \rho_0 \exp(\Delta/kT)$ (ρ_0 —resistivity at 273.15 K), where for an indirect bandgap, we obtained $\Delta \sim 0.88$ eV. The inset shows the resistivity measured vs. magnetic field at room temperature. The magnetoresistivity is positive and almost linear with the magnetic field. It is also relatively small, below 2% for 9 T.

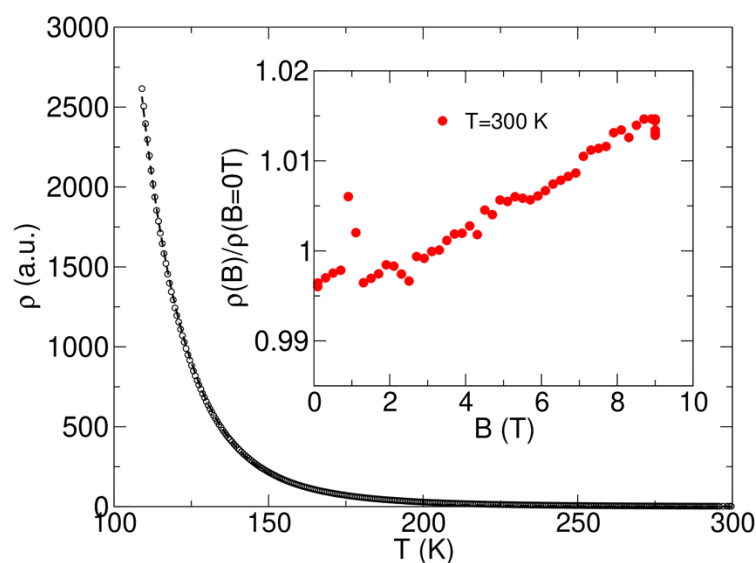


Figure 11. The resistivity of the $\text{Zn}_{0.88}\text{Pb}_{0.12}\text{Cr}_2\text{Se}_4$ single crystal measured vs. temperature (central Figure) and vs. field at $T = 300$ K (inset). The $\text{Zn}_{0.88}\text{Pb}_{0.12}\text{Cr}_2\text{Se}_4$ sample was tiny. Hence, we do not provide the absolute value of the resistivity.

3.5. Thermal Analysis

The thermal analysis examined two crystals of $\text{Zn}_{1-x}\text{Pb}_x\text{Cr}_2\text{Se}_4$ containing minimum (0.06) and maximum (0.12) lead amounts. The DSC and TG curves are depicted in Figure 12.

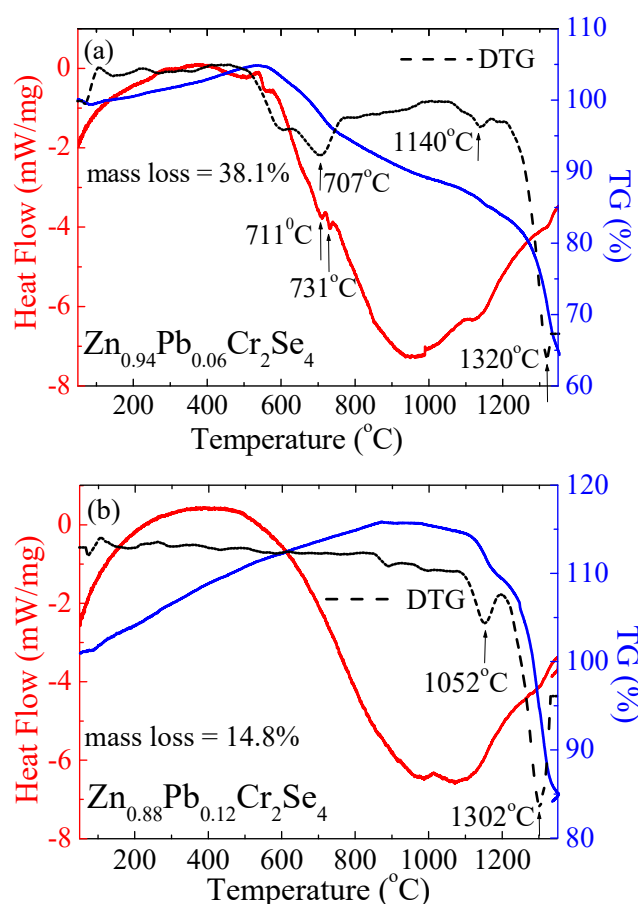


Figure 12. DSC/TG curves for $\text{Zn}_{0.94}\text{Pb}_{0.06}\text{Cr}_2\text{Se}_4$ (a) and $\text{Zn}_{0.88}\text{Pb}_{0.12}\text{Cr}_2\text{Se}_4$ (b) single crystals.

The shape of the DSC curves is similar to pure ZnCr_2Se_4 . For the sample $\text{Zn}_{0.94}\text{Pb}_{0.06}\text{Cr}_2\text{Se}_4$, two small endothermic peaks are observed at 711 °C and 733 °C. The observed peaks are in a similar position close to pure ZnCr_2Se_4 (755 °C) [44]. These peaks indicate that the melting process of the sample starts at about 711 °C. The peak confirms it on the DTG curve. However, the sample $\text{Zn}_{0.88}\text{Pb}_{0.12}\text{Cr}_2\text{Se}_4$ lacks typical endothermic peaks. On the TG curves for both samples, a few percent increase in weight is visible in the first step. This phenomenon can indicate that the investigated sample absorbs an inert gas during the heating or solid-state–gas reaction. The mass loss is observed with increasing temperature on the DTG curve. It is an endothermic reaction, as indicated by the downward deflection of the DSC curve. The partial destruction of investigated samples takes place at about 1300°C. It suggests that the samples doped with Pb are thermally more stable than pure ZnCr_2Se_4 .

4. Conclusions

In conclusion, we have demonstrated the family of $\text{Zn}_{1-x}\text{Pb}_x\text{Cr}_2\text{Se}_4$ ($x = 0.06, 0.07, 0.09, 0.11, 0.12$) spinel single crystals showing semiconducting and AFM behaviour. These single crystals were successfully obtained using chemical vapour transport. The technology of crystal growth was based on thermodynamic calculations. XRD analysis showed that these crystals possess a cubic structure (SG: $Fd3m$). Thermal analysis showed that the single crystals under study are thermally stable up to 1300°C.

With the increase in the external magnetic field, a shift of T_N and the specific heat peak towards lower temperatures and θ towards higher ones was observed, as well as a strong weakening of long-range AFM interactions visible in the reduction of the super-exchange integral for the first coordination sphere and the appearance of spin fluctuations in the paramagnetic region, visible in magnetic fields of 40 and 50 kOe. Below T_N , the magnetic field dependence of magnetisation, $M(H)$, showed two peculiarities at critical fields $H_{c1} = 12$ and $H_{c2} = 57$ kOe and a change of the sign of the J_1 -integral from negative to positive at $H_{dc} = 50$ kOe, which causes the short-range FM interaction to extend over the entire temperature range. Finally, we can conclude that doped chalcogenide spinels are suitable materials for application in many technological areas, such as magnetic materials for capacitors, transformers, or components in electronic products.

Author Contributions: Conceptualisation, I.J. and T.G. (Tadeusz Groń); methodology, I.J., T.G. (Tadeusz Groń), B.S., E.P., J.J., B.W.-K., and H.D.; validation, I.J. and T.G. (Tadeusz Groń); formal analysis, I.J., B.W.-K., and T.G. (Tadeusz Groń); investigation, I.J., Z.S., J.K., E.P., T.G. (Tomasz Goryczka), B.S., J.J., J.G., and H.D.; resources, I.J.; writing—original draft preparation, I.J., T.G. (Tadeusz Groń), and J.G.; writing—review and editing, I.J., T.G., and J.G.; visualisation, I.J. and T.G. (Tadeusz Groń); supervision, I.J.; project administration, I.J. All authors have read and agreed to the published version of the manuscript.

Funding: This study was supported by project VEGA 1/0116/22.

Institutional Review Board Statement: Not applicable.

Informed Consent Statement: Not applicable.

Data Availability Statement: Not applicable.

Conflicts of Interest: The authors declare no conflict of interest.

References

1. Hemberger, J.; von Nidda, H.-A.K.; Tsurkan, V.; Loidl, A. Large Magnetostriction and Negative Thermal Expansion in the Frustrated Antiferromagnet ZnCr_2Se_4 . *Phys. Rev. Lett.* **2007**, *98*, 147203.
2. Kondo, S.; Johnston, D.C.; Swenson, C.A.; Borsa, F.; Mahajan, A.V.; Miller, L.L.; Gu, T.; Goldman, A.I.; Maple, M.B.; Gajewski, D.A.; et al. LiV_2O_4 : A Heavy Fermion Transition Metal Oxide. *Phys. Rev. Lett.* **1997**, *78*, 3729–3732.
3. Krimmel, A.; Loidl, A.; Klemm, M.; Horn, S.; Schober, H. Dramatic Change of the Magnetic Response in LiV_2O_4 : Possible Heavy Fermion to Itinerant d -Metal Transition. *Phys. Rev. Lett.* **1999**, *82*, 2919–2922.

4. Lee, S.-H.; Broholm, C.; Ratcliff, W.; Gasparovic, G.; Huang, Q.; Kim, T.H.; Cheong, S.-W. Emergent excitations in a geometrically frustrated magnet. *Nature* **2002**, *418*, 856–858.
5. Radaelli, P.G.; Horibe, Y.; Gutmann, M.J.; Ishibashi, H.; Chen, C.H.; Ibberson, R.M.; Koyama, Y.; Hor, Y.-S.; Kiryukhin, V.; Cheong, S.-W. Formation of isomorphous Ir^{3+} and Ir^{4+} octamers and spin dimerisation in the spinel CuIr_2S_4 . *Nature* **2002**, *416*, 155–158.
6. Schmidt, M.; Ratcliff, W.; Radaelli, P.G., II; Refson, K.; Harrison, N.M.; Cheong, S.W. Spin Singlet Formation in MgTi_2O_4 : Evidence of a Helical Dimerization Pattern. *Phys. Rev. Lett.* **2004**, *92*, 056402.
7. Fritsch, V.; Hemberger, J.; Büttgen, N.; Scheidt, E.-W.; Krug von Nidda, H.-A.; Loidl, A.; Tsurkan, V. Spin and Orbital Frustration in MnSc_2S_4 and FeSc_2S_4 . *Phys. Rev. Lett.* **2004**, *92*, 116401.
8. Krimmel, A.; Mücksch, M.; Tsurkan, V.; Koza, M.M.; Mutka, H.; Loidl, A. Vibronic and Magnetic Excitations in the Spin-Orbital Liquid State of FeSc_2S_4 . *Phys. Rev. Lett.* **2005**, *94*, 237402.
9. Fichtl, R.; Tsurkan, V.; Lunkenheimer, P.; Hemberger, J.; Fritsch, V.; Krug von Nidda, H.-A.; Scheidt, E.-W.; Loidl, A. Orbital Freezing and Orbital Glass State in FeCr_2S_4 . *Phys. Rev. Lett.* **2005**, *94*, 027601.
10. Hemberger, J.; Lunkenheimer, P.; Fichtl, R.; Krug von Nidda, H.-A.; Tsurkan, V.; Loidl, A. Relaxor ferroelectricity and colossal magnetocapacitive coupling in ferromagnetic CdCr_2S_4 . *Nature* **2005**, *434*, 364–367.
11. Weber, S.; Lunkenheimer, P.; Fichtl, R.; Hemberger, J.; Tsurkan, V.; Loidl, A. Colossal Magnetocapacitance and Colossal Magnetoresistance in HgCr_2S_4 . *Phys. Rev. Lett.* **2006**, *96*, 157202.
12. Yamasaki, Y.; Miyasaka, S.; Kaneko, Y.; He, J.-P.; Arima, T.; Tokura, Y. Magnetic Reversal of the Ferroelectric Polarisation in a Multiferroic Spinel Oxide. *Phys. Rev. Lett.* **2006**, *96*, 207204.
13. Lee, S.-H.; Broholm, C.; Kim, T.H.; Ratcliff, W.; Cheong, S.-W., II. Local Spin Resonance and Spin-Peierls-like Phase Transition in a Geometrically Frustrated Antiferromagnet. *Phys. Rev. Lett.* **2000**, *84*, 3718.
14. Tchernyshyov, O.; Moessner, R.; Sondhi, S.L. Order by Distortion and String Modes in Pyrochlore Antiferromagnets. *Phys. Rev. Lett.* **2002**, *88*, 067203.
15. Yamashita, Y.; Ueda, K. Spin-Driven Jahn-Teller Distortion in a Pyrochlore System. *Phys. Rev. Lett.* **2000**, *85*, 4960.
16. Hemberger, J.; Rudolf, T.; Krug von Nidda, H.-A.; Mayr, F.; Pimenov, A.; Tsurkan, V.; Loidl, A. Spin-Driven Phonon Splitting in Bond-Frustrated ZnCr_2S_4 . *Phys. Rev. Lett.* **2006**, *97*, 087204.
17. Groń, T.; Duda, H.; Warczewski, J. Influence of the valence of the substituted cations on the electrical properties of the magnetically modulated spinels $\text{Zn}_{1-x}\text{A}_x\text{Cr}_2\text{Se}_4$ ($\text{A} = \text{Cu}, \text{Ga}_{2/3}$). *Phys. Rev.* **1990**, *41*, 12424–12431.
18. Groń, T. Influence of vacancies and mixed valence on the transport processes in solid solutions with the spinel structure. *Philos. Mag. B* **1994**, *70*, 121–132.
19. Groń, T.; Wolff, J.; Hehenkamp, Th.; Bärner, K.; Okońska-Kozłowska, I.; Jendrzewska, I.; Malicka, E. Positron annihilation studies in single and polycrystals of $\text{Zn}_{1-x}\text{Cu}_x\text{Cr}_2\text{Se}_4$ spinel series. *Radiat. Eff. Defects Solids* **1996**, *139*, 97–107.
20. Parker, D.R.; Green, M.A.; Bramwell, S.T.; Wills, A.S.; Gardner, J.S.; Neumann, D.A. Crossover from Positive to Negative Magnetoresistance in a Spinel. *J. Am. Chem. Soc.* **2004**, *126*, 2710–2711.
21. Lotgering, F.K. Ferromagnetic interactions in sulphides, selenides and tellurides with spinel structure: In Proceedings of the International Conference on Magnetism, Nottingham, UK, 7–11 September 1964; Institute of Physics and the Physical Society, London: London, UK, 1965; p. 533.
22. Plumier, R. Étude par diffraction de neutrons de l'antiferromagnétisme hélicoïdal du spinelle ZnCr_2Se_4 en présence d'un champ magnétique. *J. Phys.* **1966**, *27*, 213–219.
23. Park, S.; Kwon, S.; Lee, S.; Khim, S.; Bhoi, D.; Park, C.B.; Kim, K.H. Interactions in the bond-frustrated helimagnet ZnCr_2Se_4 investigated by NMR. *Scien. Rep.* **2019**, *9*, 16627.
24. Kleinberger, R.; de Kouchkovsky, C.R. Étude radiocristallographique à basse température du spinelle ZnCr_2Se_4 . *Acad. Sci. Paris Ser. B* **1966**, *262*, 628–630.
25. Yokaichiya, F.; Krimmel, A.; Tsurkan, V.; Margiolaki, I.; Thompson, P.; Bordallo, H.N.; Buchsteiner, A.; Stußer, N.; Argyriou, D.N.; Loidl, A. Spin-driven phase transitions in ZnCr_2Se_4 and ZnCr_2S_4 probed by high-resolution synchrotron x-ray and neutron powder diffraction. *Phys. Rev. B* **2009**, *79*, 064423.
26. Malicka, E.; Groń, T.; Pacyna, A.W.; Maciążek, E.; Duda, H.; Pawełczyk, M.; Zawisza, B.; Sitko, R. Influence of temperature on the critical fields in $\text{ZnCr}_{2-x}\text{Al}_x\text{Se}_4$ antiferromagnets. *J. Alloys Compd.* **2009**, *480*, 67–69.
27. Groń, T.; Malicka, E.; Duda, H.; Pacyna, A.W.; Mydlarz, T.; Sitko, R.; Pawełczyk, M. Spin-glass-like behavior in $\text{Zn}_x\text{Cr}_y\text{Al}_z\text{Se}_4$. *J. Phys. Chem. Sol.* **2009**, *70*, 1175–1180.
28. Malicka, E.; Groń, T.; Ślebarski, A.; Pacyna, A.W.; Goraus, J.; Fijałkowski, M.; Heimann, J. Specific heat and magnetic susceptibility of single-crystalline $\text{ZnCr}_{2-x}\text{Al}_x\text{Se}_4$ ($x = 0.15, 0.23$). *J. Phys. Chem. Sol.* **2011**, *72*, 974–979.
29. Groń, T.; Jendrzewska, I.; Gołabek, S.; Duda, H.; Krajewski, A.; Bärner, K. The thermoelectric power of ferromagnetically ordered $\text{Zn}_x\text{Cu}_y\text{Cr}_z\text{Se}_4$ single crystals. *Physica B* **2003**, *327*, 88–95.
30. Mazur, S.; Groń, T.; Jendrzewska, I. Influence of spin arrangement on thermopower in $\text{Zn}_x\text{Cu}_y\text{Cr}_z\text{Se}_4$ spinels. *J. Alloys Compd.* **2009**, *480*, 19–22.
31. Okońska-Kozłowska, I.; Lutz, H.D.; Groń, T.; Krok, J.; Mydlarz, T. Darstellung, elektrische und magnetische Eigenschaften von $\text{Zn}_{1-x}\text{Ga}_{0.667x}\text{Cr}_2\text{Se}_4$ -Spinel-Einkristallen. *Mater. Res. Bull.* **1984**, *19*, 1–5.
32. Groń, T.; Duda, H.; Warczewski, J. Transport phenomena in the antiferromagnetic spinels $\text{Zn}_{1-x}\text{Ga}_{2x/3}\text{Cr}_2\text{Se}_4$ (where $0.0 < x < 0.5$). *J. Mag. Mag. Mater.* **1990**, *83*, 487–489.

33. Malicka, E.; Groń, T.; Ślebarski, A.; Gagor, A.; Pacyna, A.W.; Sitko, R.; Goraus, J.; Mydlarz, T.; Heimann, J. Specific heat and magnetic susceptibility of single-crystalline ZnCr_2Se_4 spinels doped with Ga, In and Ce. *Mater. Chem. Phys.* **2011**, *131*, 142–150.
34. Groń, T.; Kopyczok, J.; Okońska-Kozłowska, I.; Warczewski, J. Seebeck effect in the antiferromagnetic single crystals of $\text{ZnCr}_{2-x}\text{In}_x\text{Se}_4$ ($0.0 < x < 0.15$). *J. Mag. Mag. Mater.* **1992**, *111*, 53–55.
35. Jendrzewska, I.; Groń, T.; Kusz, J.; Żelechower, M.; Maciążek, E.; Ślebarski, A.; Fijałkowski, M. Spin-glass-like behaviour in tin doped ZnCr_2Se_4 single crystals. *J. Alloys Compd.* **2015**, *635*, 238–244.
36. Jendrzewska, I.; Mroziński, J.; Groń, T.; Duda, H.; Zajdel, P.; Pacyna, A.W.; Maciążek, E.; Hanc, A. Effect of cation substitution on Fermi level of n-type $\text{Zn}_x\text{Sn}_y\text{Cr}_z\text{Se}_4$ spinels. *J. Alloys Compd.* **2009**, *480*, 63–66.
37. Jendrzewska, I.; Groń, T.; Kwapuliński, P.; Kusz, J.; Pietrasik, E.; Goryczka, T.; Sawicki, B.; Ślebarski, A.; Fijałkowski, M.; Jampilek, J.; et al. Study of the structure, magnetic, thermal and electrical characterisation of $\text{ZnCr}_2\text{Se}_4\text{:Ta}$ single crystals obtained by chemical vapour transport. *Materials* **2021**, *14*, 2749.
38. Jendrzewska, I.; Groń, T.; Knizek, K.; Pilch, M.; Ślebarski, A.; Goraus, J.; Zajdel, P.; Stokłosa, Z.; Pietrasik, E.; Goryczka, T.; et al. Preparation, structure and magnetic, electronic and thermal properties of Dy^{3+} -doped ZnCr_2Se_4 with unique geometric type spin-glass. *J. Sol. State Chem.* **2021**, *298*, 122114.
39. Jendrzewska, I.; Groń, T.; Maciążek, E.; Duda, H.; Kubisztal, M.; Ślebarski, A.; Pietrasik, E.; Fijałkowski, M. Specific heat and magnetic properties of single-crystalline $\text{Zn}_x\text{Dy}_y\text{Cr}_z\text{Se}_4$ spinels. *J. Mag. Mag. Mater.* **2016**, *407*, 122–128.
40. Maciążek, E.; Karolus, M.; Kubisztal, M.; Jendrzewska, I.; Sitko, R.; Groń, T.; Ślebarski, A.; Fijałkowski, M. Magnetic and specific heat properties of a new Gd-doped ZnCr_2Se_4 . *Mater. Chem. Phys.* **2015**, *168*, 187–192.
41. Jendrzewska, I.; Groń, T.; Kusz, J.; Goraus, J.; Barsova, Z.; Pietrasik, E.; Czerniewski, J.; Goryczka, T.; Kubisztal, M. Growth, structure and physico-chemical properties of monocrystalline $\text{ZnCr}_2\text{Se}_4\text{:Ho}$ prepared by chemical vapour transport. *J. Sol. State Chem.* **2020**, *281*, 121024.
42. Jendrzewska, I.; Groń, T.; Goraus, J.; Pilch, M.; Pietrasik, E.; Barsova, Z.; Czerniewski, J.; Goryczka, T.; Witkowska-Kita, B.; Bienko, A.; et al. Synthesis and structural, magnetic, thermal and electronic properties of Mn-doped ZnCr_2Se_4 . *Mater. Chem. Phys.* **2019**, *238*, 121901.
43. Jendrzewska, I.; Zajdel, P.; Heimann, J.; Krok-Kowalski, J.; Mydlarz, T.; Mrzigod, J. Influence of manganese on magnetic and electronic properties of ZnCr_2Se_4 single Crystals. *Mater. Res. Bull.* **2012**, *47*, 1881–1886.
44. Jendrzewska, I.; Groń, T.; Kusz, J.; Barsova, Z.; Pietrasik, E.; Goryczka, T.; Sawicki, B.; Ślebarski, A.; Fijałkowski, M.; Jampilek, J.; et al. Synthesis, crystal structure and characterization of monocrystalline ZnCr_2Se_4 doped with neodymium. *J. Sol. State Chem.* **2020**, *292*, 121661.
45. Jendrzewska, I.; Waśkowska, A.; Mydlarz, T. Influence of nickel substitution on the cation distribution and magnetic properties of ZnCr_2Se_4 . *J. Alloys Compd.* **2001**, *327*, 73–77.
46. Lenz, M.; Gruhn, R. Developments in Measuring and Calculating Chemical Vapor Transport Phenomena Demonstrated on Cr, Mo, W and Their Compounds. *Chem. Rev.* **1997**, *97*, 2967–2994.
47. Plies, V. Massenspektrometrische Untersuchungen der Gasphase über CrCl_3 und $\text{CrCl}_3/\text{Cl}_2$. *Zeitschrift für anorganische und allgemeine Chemie* **1988**, *556*, 120–128.
48. Sheldrick, G.M. Crystal structure refinement with SHELXL. *Acta Cryst.* **2015**, *C71*, 3–8.
49. Morrish, A.H. *Physical Principles of Magnetism*; John Wiley & Sons, Inc.: New York, NY, USA, 1965.
50. Holland, W.E.; Brown, H.A. Application of the Weiss molecular field theory to the B-site spinel. *Phys. Status Solidi* **1972**, *10*, 249–253.
51. Shannon, R.D. Revised Effective Ionic Radii and Systematic Studies of Interatomic Distances in Halides and Chalcogenides. *Acta Cryst.* **1976**, *A32*, 751–767.